3D printing of porcelain and finite element simulation of sintering affected by final stage pore gas pressure

Charles Manière, Christelle Harnois, Sylvain Marinel

3D printing of porcelain and finite element simulation of sintering affected by final stage pore gas pressure

Charles Manière[1]*, Christelle Harnois[1], Sylvain Marinel[1]

1. Normandie Univ, ENSICAEN, UNICAEN, CNRS, CRISMAT, 14000, Caen, France

Keywords

3D printing; ceramic; simulation; sintering; swelling

Abstract

Ceramic 3D printing involves various sintering phenomena such as shape distortions, crack formations, shrinkage anisotropy, and residual porosity that demands the development of a simulation tool. Moreover, liquid-phase sintering of materials such as porcelain exhibits an additional and challenging phenomenon at the end of the sintering process that reflects closed porosity growth and coalescence owing to the pressure created by the pore-trapped gases, which further implies swelling (or bloating) of the entire specimen accompanied by distortions. In this study, the swelling issue of 3D-printed porcelain samples was investigated through a sintering dilatometry parametric design to determine the optimal heating rate and holding temperature. A sintering modeling theory was employed to characterize the final stage pore gas pressure via an inverted sintering model formulation. Finally, a finite element sintering simulation was applied based on the analytical model data to predict the sintering shrinkage of a complex geometry.

Graphical Abstract

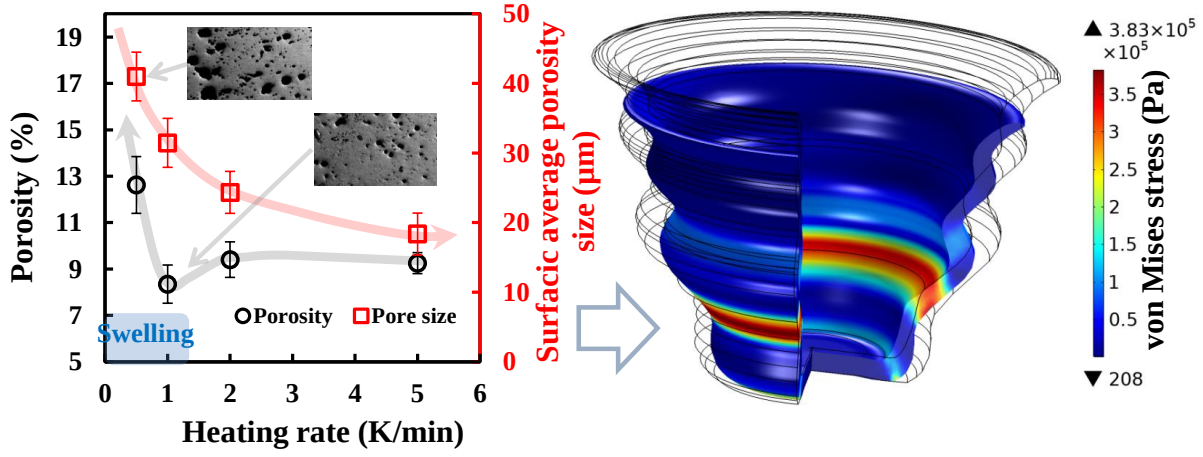

* Corresponding author: **CM**: Laboratoire de cristallographie et sciences des matériaux (CRISMAT), 6 Bvd du maréchal Juin 14050 CAEN CEDEX 4, France

Ph.: +33.2.31.45.13.69 ; *E-mail address*: charles.maniere@ensicaen.fr

Nomenclature

θ Porosity

$\dot{\theta}$ Porosity elimination rate (s^{-1})

$\underline{\sigma}$ Stress tensor ($N.m^{-2}$)

$\underline{\dot{\varepsilon}}$ Strain rate tensor (s^{-1})

$\dot{e}$ The trace of the strain rate tensor (s^{-1})

φ Shear modulus

ψ Bulk modulus

Pl Sintering stress (Pa)

P_s Inner pore gas pressure (Pa)

$\mathbb{i}$ Identity tensor

α Surface energy ($J.m^{-2}$)

r Particle radius (m)

η Material viscosity (Pa.s)

η_0 Viscosity pre-exponential factor (Pa s K^{-1})

Q Viscosity activation energy ($J.mol^{-1}$)

R Gas constant 8.314 ($J.mol^{-1}.K^{-1}$)

T Temperature (K)

h Specimen height (mm)

h_0 Initial specimen height (mm)

1. Introduction

Ceramic 3D printing incorporates numerous manufacturing methods that possess the potential for fully automated production of ceramic objects. Thus, in an attempt to drive this objective to an unprecedented level, dedicated efforts have been oriented toward multi-material additive manufacturing via combined additive methods [1]. Apart from powder bed fusion [2], ceramic 3D printing/additive manufacturing is essentially a green specimen printing method [3,4] by opposition to subtractive shaping methods. A general description of the commonly used methods are stated as follows. Material extrusion methods are based on the direct deposition of a ceramic paste with a resolution between 0.4–1 mm. They are

generally called “robocasting” but are also termed as ”fused deposition modeling” when a ceramic/polymer filament is used [5]. Stereolithography is a method based on selective vat photopolymerization of a ceramic paste that allows attaining resolutions as low as 10–100 µm [1,6]. Furthermore, the binder jetting methods can be cited powder bed-based methods that allow a resolution of approximately 50 µm by liquid bonding agent [7]. Among all these methods, our study is based on the robocasting method, which provides the advantages of fast printing, low material losses, and cheap equipment. However, the disadvantages include poor resolution and rough surface owing to the printing rods, and the success of printing is directly linked to paste rheology and printing conditions [5]. Thus, different strategies have been developed for the paste to resist deformations and gravity slumping after printing [8]; these are based on fusion–solidification, rapid solvent drying, gelation [9] after printing, or using a paste with sufficient yield stress to support layer stacking and exhibit shear-thinning flow behavior [10].

The sintering of printed specimens is also a critical aspect that may suffer from deformations if the shapes are not sufficiently supported [11] or have small wall thickness, low filling density [12], and anisotropy [13,14]. In general, these distortions result from the gravity or friction against the supports of weak and heavy structures [15]. Further, these problems can become predominant for materials with very low viscosity at sintering temperatures, such as liquid-phase sintering [16]. Therefore, finite element simulation poses as a precisely efficient tool to predict the sintering distortion of weak structures [17,18]. Besides, cracks constitute as another type of defects that may occur from both debinding and sintering. Apart from multi-material sintering, cracks mainly originate from high print volumes and heterogeneous heating. Moreover, a high wall thickness may generate cracks through the internal gas produced by the organic phase decomposition in debinding [19,20]. Similarly, a high print volume may generate temperature gradients between the core and the edge, thus resulting in heterogeneous shrinkage fields and crack formation during sintering. In this case, a simulation tool may be used to predict the stress generated by the thermal gradient

[21]. Concerning the liquid-phase sintering of porcelain, another important source of homogeneity is the swelling (or bloating) effect caused by the gases trapped in the pores. This phenomenon is very active when the liquid phase starts to close the porosity [22]. The trapped gases can be eliminated only through the solubility of the gases in the lattice or grain boundaries. For insoluble gases, sintering stops at a certain critical porosity; for partially soluble gases, densification followed by swelling can be observed. In addition, the transport of partially soluble gases from one pore to another may generate pore growth and pore coalescence phenomena [23,24]. Similarly, swelling and pore growth phenomena are typically observed in porcelain/clay sintering [25,26]. These phenomena may be further amplified through pollution and changes in the element valence, which releases gases such as iron (+III, +II) [27,28]. Similarly, for liquid-phase sintering of Si_3N_4, the swelling phenomenon originates from the material decomposition occurring near 1900 °C [29].

Therefore, this study is oriented toward the negation of the swelling phenomenon appearing in the final stage of the printed green porcelain specimens. Special considerations were made to identify the impact of 3D printing layered structures on the porosity distribution of the sintered samples. Furthermore, dilatometry exploration was used to determine the optimal heating rate and holding temperature [22]. Moreover, a theoretical approach was employed to determine the sintering model parameters involving the trapped gas pressure [30]. Subsequently, these data were used for the finite element simulation of a thin-wall complex printed shape sintering.

2. Theory and calculations

The sintering model was first detailed in an analytical approach for determining the sintering/pore gas pressure parameters. Subsequently, the sintering model was detailed by the general continuum theory of sintering for the finite element sintering simulation of the printed cup.

The continuum theory of sintering [31] can be reduced to an analytical equation describing pressureless sintering:

$$-P_l = \frac{2\eta\psi\dot{\theta}}{(1-\theta)} \quad (1)$$

where the terms P_l and ψ can be theoretically defined [32] as

$$P_l = \frac{3\alpha(1-\theta)^2}{r} \quad (2)$$

$$\psi = \frac{2(1-\theta)^3}{3\theta} \quad (3).$$

The viscosity–temperature dependence was expressed by [31,33]:

$$2\eta = \eta_0 T exp\left(\frac{Q}{RT}\right) \quad (4).$$

Therefore, combining Equations (2), (3), and (4) with (1), we obtained the analytical pressureless sintering expression (5) with the unknown isolated viscosity terms η_0, α, and Q.

$$\frac{-3(1-\theta)^3}{rT\psi\dot{\theta}} = \frac{\eta_0}{\alpha} exp\left(\frac{Q}{RT}\right) \quad (5)$$

The logarithmic form of the above equation yields Equation (6), where it is possible to determine the ratio η_0/α and the activation energy Q through linear regression. In general, this determination was made in the initial and intermediate stages of sintering to avoid disturbances from the grain growth or the closed pore inner gas pressure.

$$ln\left(\frac{-3(1-\theta)^3}{rT\psi\dot{\theta}}\right) = ln\left(\frac{\eta_0}{\alpha}\right) + \frac{Q}{RT} \quad (6)$$

The left-hand side of the above equation can be computed from the experimental data versus *1/RT* to identify the activation energy Q and the term η_0/α. The swelling phenomenon during the final stage of sintering of liquid phase sintering requires considering the inner closed pore gas pressure P_s. The sintering model (1) was modified to Equation (7) for considering P_s, which opposes the sintering stress P_l. The swelling phenomenon implied the expansion of the specimen when $P_s > P_l$. However, the pore gas pressure can significantly decrease the densification kinetics even for $P_s < P_l$.

$$P_s - P_l = \frac{2\eta\psi\dot{\theta}}{(1-\theta)} \quad (7)$$

The gas pressure P_s may evolve with the sample temperature and time. Therefore, the inner gas pressure can be determined from the final stage of sintering dilatometry data and the previously determined sintering parameters Q and η_0/α for open porosity. The inner gas pressure identification equation used to determine P_s/α is as follows.

$$\frac{P_S}{\alpha} = \frac{\eta_0}{\alpha} exp\left(\frac{Q}{RT}\right)\frac{T\psi\dot{\theta}}{(1-\theta)} + \frac{3(1-\theta)^2}{r} \quad (8)$$

Consequently, the sintering parameters Q and η_0/α from the open porosity domain and P_s/α from the final stage can be utilized to model the liquid-phase sintering in a finite element code using the general continuum sintering theory equation:

$$\underline{\sigma} = 2\eta\left(\varphi\underline{\dot{\varepsilon}} + \left(\psi - \frac{1}{3}\varphi\right)\dot{e}\mathbb{i}\right) + (P_l - P_S)\mathbb{i} \quad (9).$$

3. Experiment and method

The sintering dilatometry tests were conducted on the dilatometer "Setaram TMA 92". The true strain was calculated from the specimen height shrinkage curve using the logarithmic relation $\ln(h/h_0)$. The cylindrical porcelain specimens were 10 mm in both diameter and height and were printed using the robocasting printing device "Delta WASP 2040 Clay" with the "CERADEL" porcelain paste "PT010B" as feedstock. The extrusion of the paste was improved by adding 5% water, as recommended by the manufacturer. The printing conditions constituted: nozzle size 1.2 mm, layer height 0.5 mm, print speed 50 mm/s, extrusion gas pressure 4 bar, shell thickness 2.4 mm, bottom/top thickness 2 mm, and filling density 100%. The optimal sintering cycle of as built part was determined by experimenting with different cycles at constant heating rates of 0.5, 1, 2, and 5 K/min toward 1300 °C. The density of the specimen was measured using Archimedes' method, and the polished microstructures were analyzed by optical (Olympus BX53M) and scanning electron microscopy (SEM/EDS map) (Jeol 7002). The thermogravimetric–differential scanning calorimetry (TG–DSC) of the powder was tested in air up to 1300 °C using the "Netzsch STA449 F3" thermal analysis apparatus.

The determination of the sintering model parameters was based on the optimized cycle, which is 1 k/min, 2 h at 1200 °C. In addition, the viscosity–temperature dependence was identified in the open porosity zone using Equation (6). Thereafter, the final stage sintering pore gas pressure was deduced from the dilatometry curve and Equation (8).

4. Results and discussions

In this section, we present the experimental determination of the optimal sintering cycle, identification of the sintering analytical modeling parameters affected by the pore gas pressure, and finally, the finite element simulation study of a complex printed shape.

4.1. TG–DSC of the powder

The thermogravimetric (TG) and differential thermal analysis (DTA) of the porcelain paste under air are reported in Figure 1. Typically, two main phenomena were detected through the analysis. The dihydroxylation of kaolinite to metakalolin took place around 550 °C accompanied by an endothermic DTA peak. This phenomenon was accompanied by a weight loss of 8%, which is close to weight loss of 7.2% announced by the manufacturer on ignition. Knowing from Carty and Senapati [34], the weight loss of pure kaolinite was approximately 14%, and we had deduced an initial kaolinite proportion of about 50% in the initial porcelain formulation. Moreover, the exothermic peak around 1000 °C was typically associated with spinel aluminosilicate and primarily the mullite phase formation [34,35].

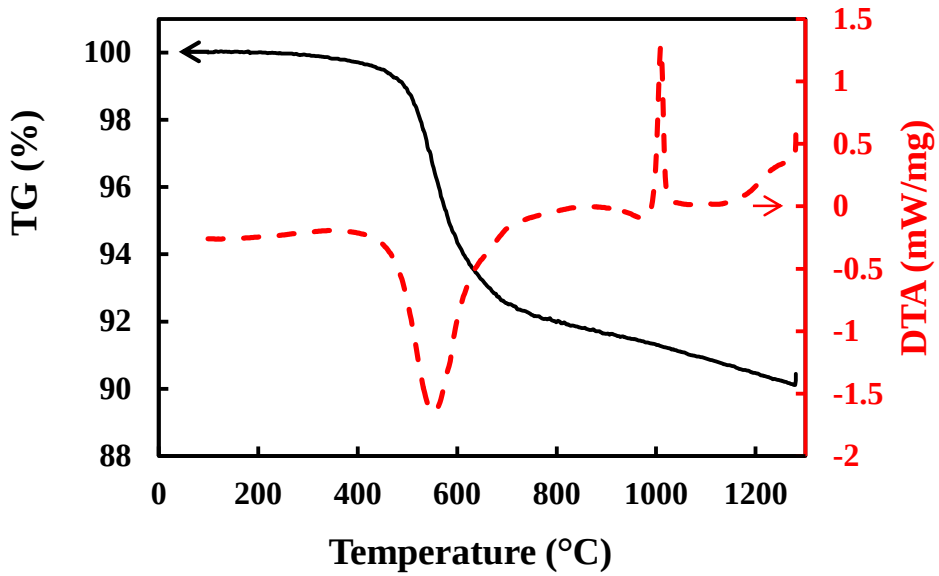

Figure 1 Thermogravimetric (TG) and differential thermal analysis (DTA) curves of the powder under air atmosphere.

4.2. Constant heating rate sintering dilatometry

In order to estimate the optimal sintering conditions of as built shapes, constant-heating rate dilatometry tests were performed up to 1300 °C. The dilatometry curves are shown in Figure 2 with in the inset, a fracture image of the initial green stage showing no filling gaps. Initially, the phenomenon detected at 1000 °C generated a small inflection of a few percent of densification on the DTA curve. As expected, the sintering curves at the intermediate stage were ordered from low to high sintering temperatures (for low to high heating rates). The final stage of sintering was the key optimization step; a swelling also called a bloating phenomenon was present, and it was responsible for lowering the sintering kinetics and the inverted densification phenomenon at 1250–1300 °C. Depending on the heating rate, the onset of this phenomenon corresponded to different temperatures: 1250 °C for 0.5 K/min, 1270 °C for 1 K/min, and 1300 °C for 2 K/min. Furthermore, the maximum shrinkage seemed to be significantly influenced by the heating rate, the optimum corresponding to 1 K/min.

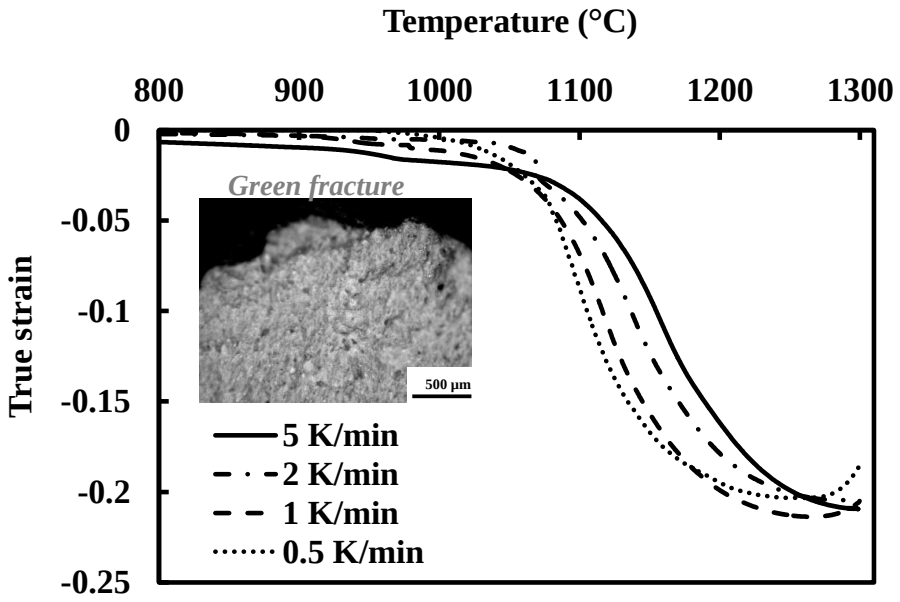

Figure 2 Constant heating rate sintering dilatometry curves of the printed specimens and in the insert the green fracture image showing not interlayer gaps.

The sintered polished microstructures were analyzed under optical microscopy to characterize the impact of the swelling phenomenon on the porosity. In addition, a pore-growth phenomenon can be evidently observed from the results presented in Figure 3. The apparent pore size was measured by surface average calculation to quantify the pore-growth phenomenon without any disturbance from the factor of low porosity. Thereafter, the 2D-apparent pore size was converted into an effective 3D-average pore size via a $4/\pi$ stereological factor assuming spherical porosity [36]. As previously discussed in the Introduction, the pore growth can originate from trapped gases in close porosity [22,25,27] and may be accompanied by a pore coalescence phenomenon depending on the solubility of the gas in the solid phase [24]. The influence of mixed valency compounds, such as iron oxide, may also release gas and generate pore swelling [28]. The red tendency curve in Figure 3 indicates that the pore growth/coalescence was directly correlated to the sintering time, i.e., a longer sintering time results in higher pore growth/coalescence phenomenon. Concerning the overall porosity evolution (gray curve in Figure 3), the densification level results from a competition between the mass transport filling the porosity in an increasing sintering time and the trapped gas that opposes the sintering capillarity driving forces. An

optimum experimental observation was obtained at 1 K/min. The overall densification was higher for the trapped gas despite the noticeable pore growth. In order to attain higher densification with lower pore growth/coalescence phenomenon, a second optimization study using an additional holding of 2 h has been detailed in the subsequent section 4.4.

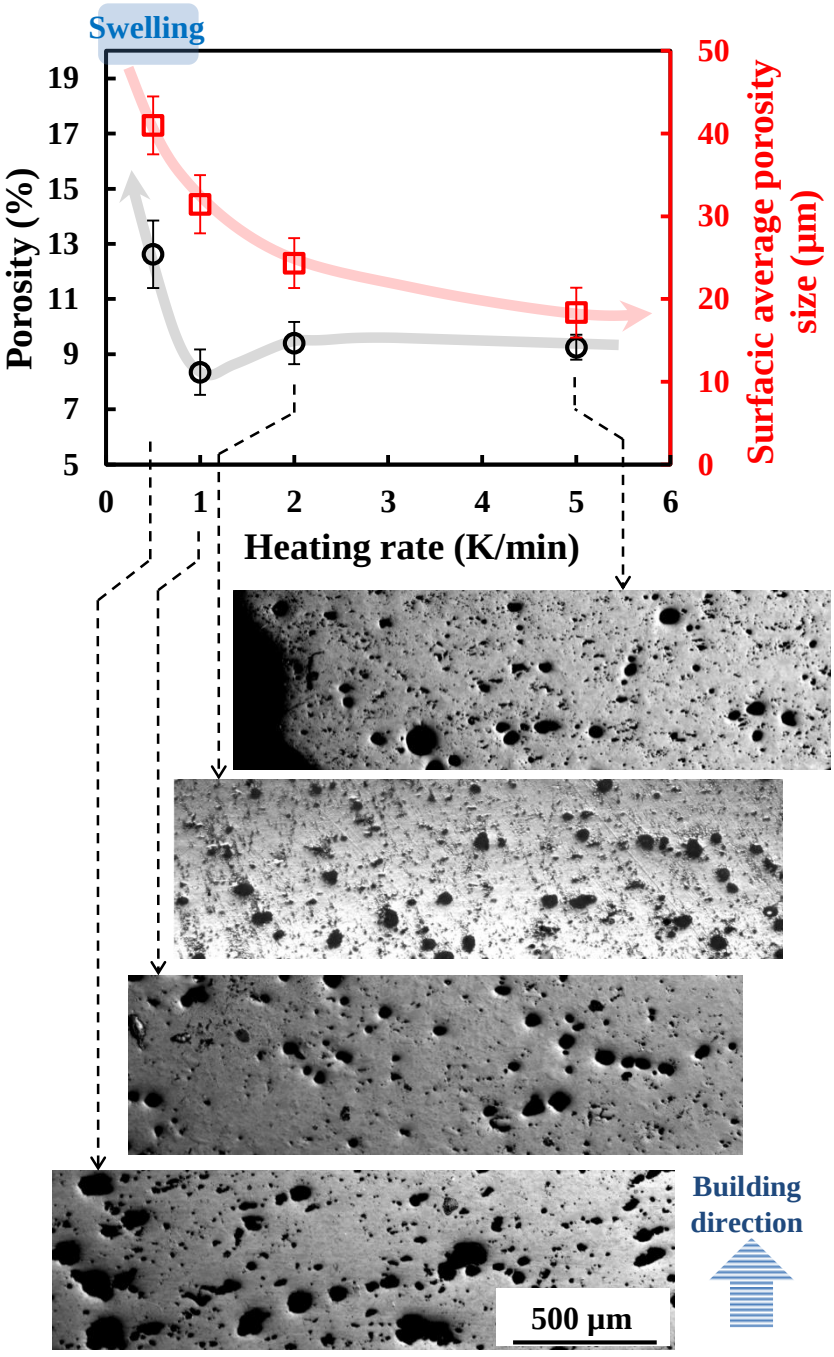

Figure 3 Microstructure analysis of the dilatometry experiments.

In the following subsection, the sintered microstructure is described based on EDS map.

4.3. EDS map analysis of the sintered specimens

The energy-dispersive X-ray spectroscopy (EDS) map near the interlayer (Figure 4) and the EDS spectrum of the main microstructural elements (Figure 5) were used to analyze the microstructures of the sintered specimens. The EDS map showed the distribution of Si, Al, K, Na, and Mg as the majorly detected elements. A line representing both very large and small pores was present at the interlayer interface. The printing conditions seemed to induce a higher content of porosity between the layers with a significant local pore growth/coalescence phenomenon as no significant gaps are observed between the rods at the green stage (figure 2). The microstructure comprised a glassy phase containing mainly Al and Si and small amounts of Na, Mg, and K surrounding the Si-rich phase. The latter corresponds to silica lumps that are typically added in the porcelain composition as a reinforcing agent.

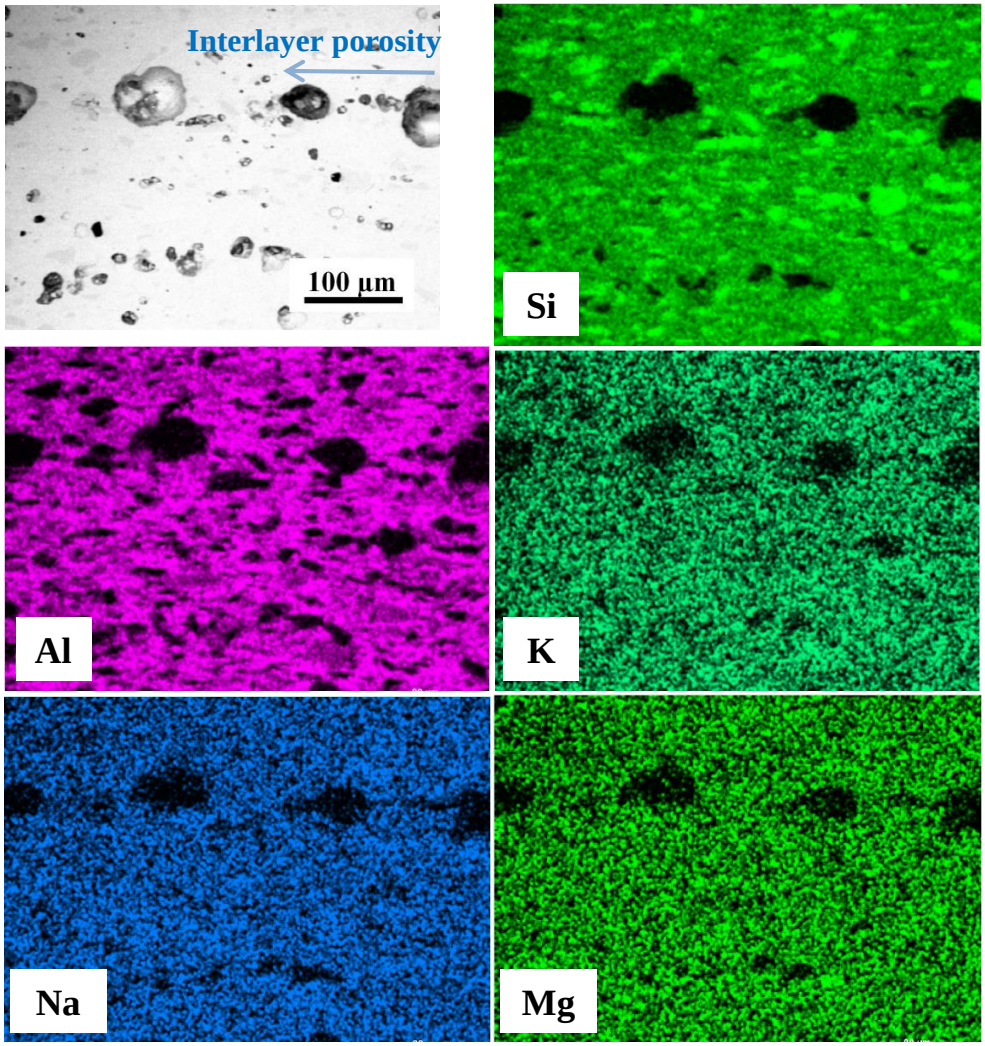

Figure 4 EDS map of the porcelain specimen in the interlayer region.

In Figure 5, different EDS spectra were recorded at different locations to detect the presence of impurities in the vicinity of the pore surfaces as well as in the bulk. The atomic percentages in the glassy phase were 63.50 % of Si, 30.17 % of Al, and small amounts of Na, Mg, and K. The silicon content was slightly higher near the porosity and very high in the gray region, thus confirming the presence of silica lumps as highlighted in the EDS map.

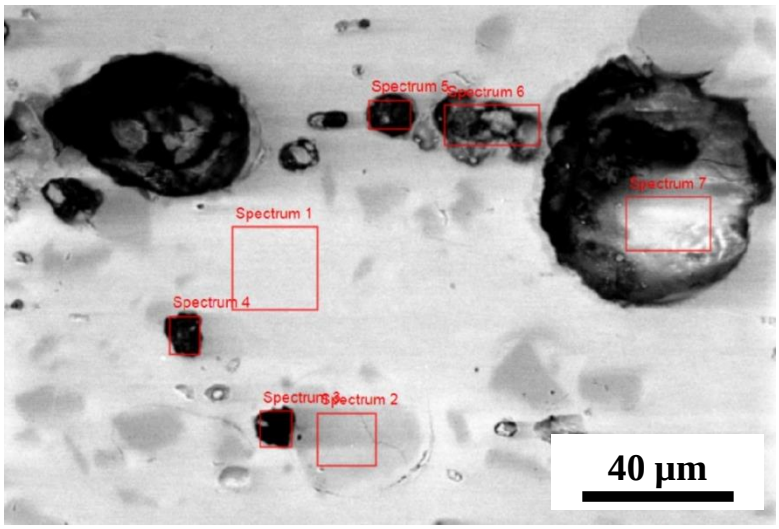

At %	Si	Al	Na	Mg	K
Spectrum 1	63,50	30,17	1,74	0,24	4,36
Spectrum 2	89,38	8,27	0,57	0,20	1,58
Spectrum 3	72,72	20,67	2,02	0,35	4,23
Spectrum 4	70,24	24,71	1,47	0,25	3,33
Spectrum 5	69,18	24,90	1,61	0,41	3,90
Spectrum 6	67,72	25,84	1,65	0,87	3,92
Spectrum 7	65,49	27,92	1,59	0,35	4,64

Figure 5 EDS analysis of the different microstructures phases/regions.

The EDS study did not provide evidence of isolated impurities that could explain the final stage of sintering swelling, which must originate from the gases trapped in the liquid phase and the early closure of pores by the smooth spherical porous shape. Therefore, the key

consideration and effect of heating rates in pore closure was detailed in the following subsection to search for the sintering optimization conditions.

4.4. Sintering cycle optimization

Based on previous sections and the dilatometry data, the optimization of the sintering process can be oriented on the adjustment of the heating rates, especially in the pore closure region. This requires ensuring optimum densification with precise adjustments of the overall heating cycle to avoid the swelling phenomenon. Based on the constant-heating rate dilatometry data shown in Figure 2, three additional dilatometry tests were conducted with the temperatures held for 2 h. The cycle at 2 K/min seemed to reach a plateau at 1300 °C, as shown in Figure 2; thus, a holding time of 2 h was further added at 1300 °C to check the densification of the structures. The results are reported in Figure 6a. During the hold, a significant swelling of about 10% was observed with an exaggerated pore size growth and an exceedingly broad pore size distribution, as shown in Figure 7a. The optimal densification was observed during the beginning of the hold. This local porosity minimum was the outcome of the competition between the trapped gas pressure and the sintering capillarity forces. Therefore, the temperature of 1300 °C must be avoided, as described in Figure 6a. In the subsequent tests, the holding temperature was imposed at a temperature slightly lower than where the minimum overall porosity was previously obtained for the test in Figure 2. The objective is to slow down the densification process right before the temperature range that corresponded to active pore closure. This strategy was applied to 5 K/min (the fastest heating rate) and to 1 K/min (the heating rate with optimum densification in Figure 2). The holding temperatures of 1250 °C and 1200 °C were selected for heating rates of 5 K/min and 1 K/min, respectively, to ensure that the holding stage starts in the densification regime (as previously shown in Figure 2). The resulting curves are shown in Figure 6b and 6c. Both the curves improved their

densification during the holding temperature without swelling; the test at 1200 °C for 1 K/min exhibited the highest densification shrinkage.

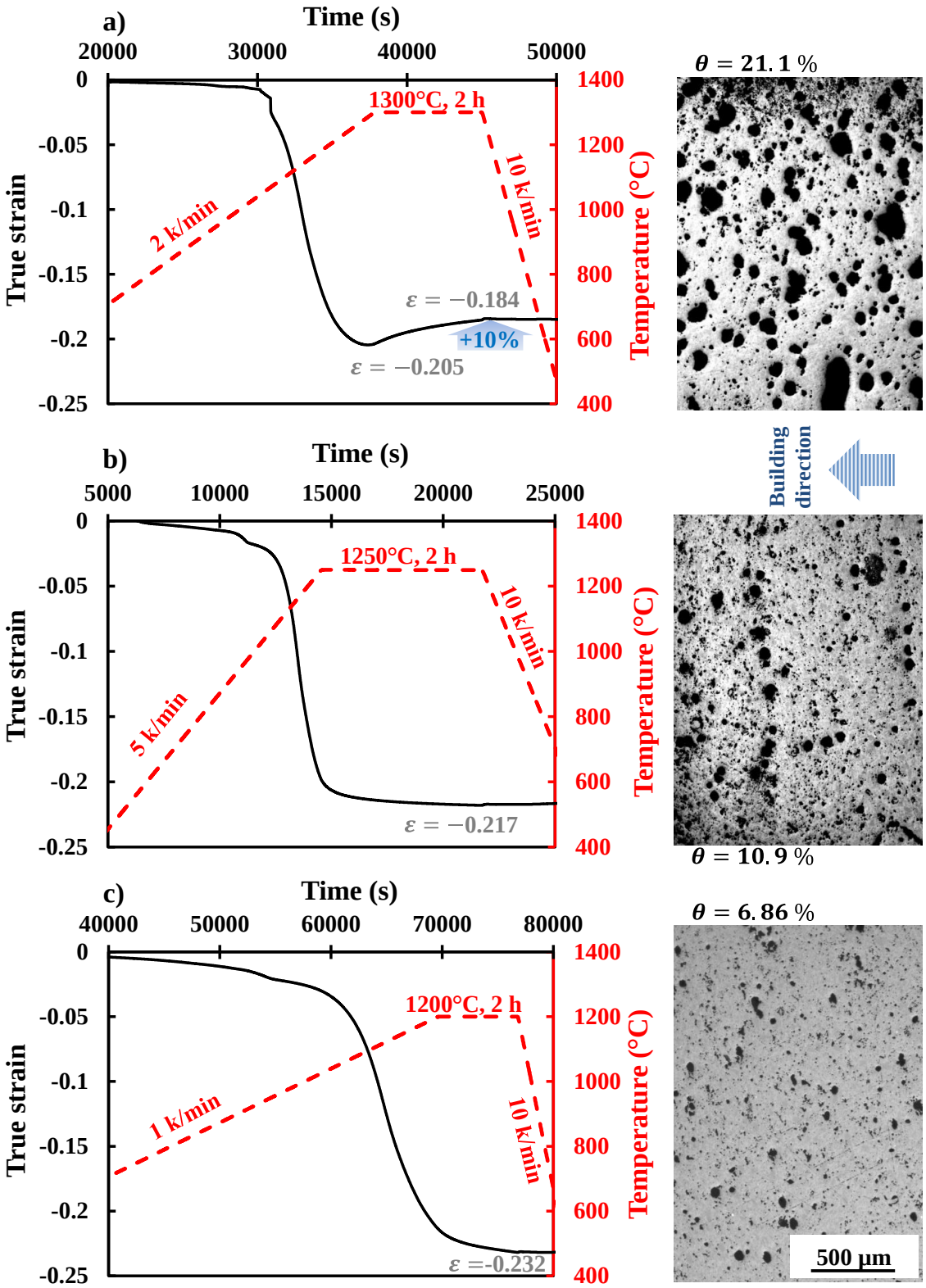

Figure 6 Optimization sintering dilatometry tests with the corresponding microstructures (right) for 2 h holding; a) 2K/min, 1300 °C, b) 5 K/min, 1250°C, c) 1 k/min, 1200 °C.

The microstructure showed a certain level of pore growth without swelling at 5 K/min, whereas the lowest pore growth levels among all the experiments were reported for the test with 1 K/min heating rate. Furthermore, the pore size distribution corresponding to 1 K/min at 1200 °C holding temperature manifested a much lower proportion of large-sized pores than the other thermal cycles showing in Figure 7a–c. The 1 K/min test demonstrated the best properties among all the studies and was treated as the reference cycle for the analytic and finite element sintering modeling.

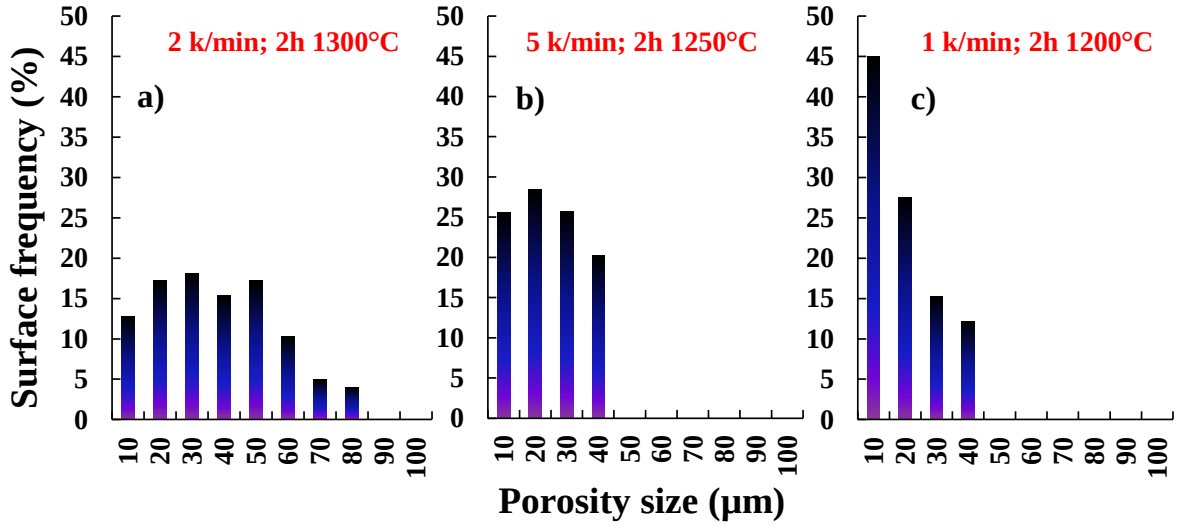

Figure 7 Pore size histogram by pore surface frequency.

4.5. Sintering analytical model and determination of viscosity and final stage sintering inner pore gas pressure.

The experimental porosity curve was calculated from the shrinkage curve of Figure 6c and is shown in Figure 8a. In order to extract suitable sintering model parameters from this curve, a direct method was employed by separately identifying the unknown viscosity–temperature dependence in the open porosity zone (initial and intermediate sintering) and the contrasting closed porosity pressure at the final stage. The onset of the active closed porosity gas pressure indicated the slowing down of the sintering curve at a critical porosity of 20 % (refer the two identification zones in Figure 8a).

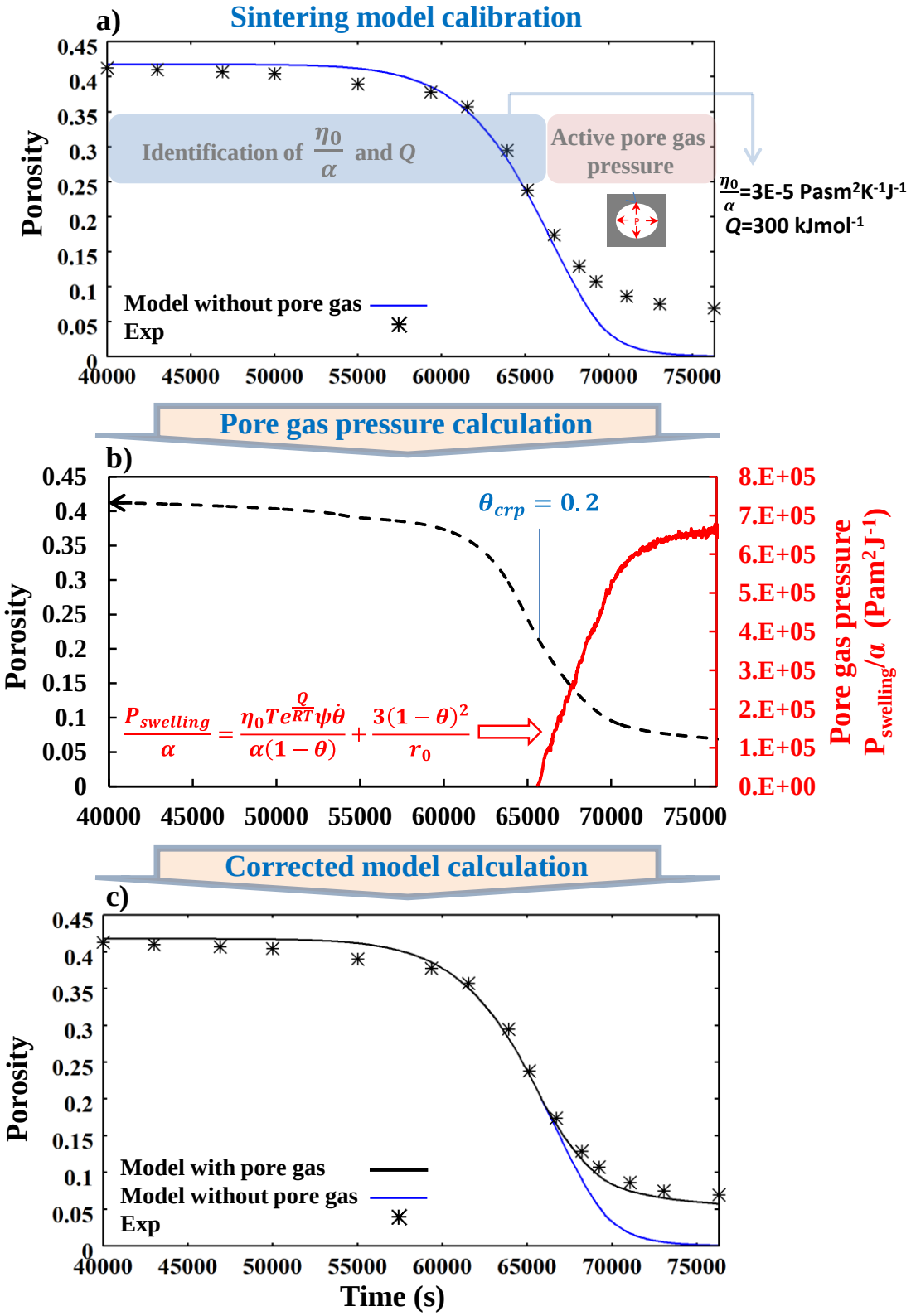

Figure 8 Sintering model parameters identification: a) viscosity parameters identification, b) pore gas pressure determination, and c) model verification.

Based on the identification Equation (6), the viscosity parameters were identified in the blue zone (see Figure 8a). An activation energy of 300 kJmol^{-1} and a pre-exponential factor of 3.00E-5 Pa·m^{2}K^{-1}J^{-1} were obtained that also included the surface energy value to avoid the

consideration of a theoretical value. Thus, this primary identification can lead to the calculation of the sintering response using Equation (1) and ignoring the final stage pore gas (blue curve in Figure 8a). As expected, the obtained model delivered a good prediction of the porosity curve in the initial and intermediate stage sintering. The model predicted the hypothetical densification response in the final stage of sintering without the presence of any trapped gases in the pores. The evolution of the effective inner pore gas pressure could be estimated using Equation (8) to correct the final stage (blue curve) in Figure 8a. Besides, such an approach assumed that the effective trapped gas pressure was the only active phenomenon that slowed down the sintering. The obtained trapped gas pressure curve is depicted in Figure 8b, which includes the surface energy term for identification and directly avoid considering a theoretical value as similar to the viscosity pre-exponential parameter. The trapped gas pressure competing with the capillarity sintering forces was slightly lower than 1 MPa assuming a surface energy close to 1 J/m^2 [37]. The analytical model influenced by the pore gas pressure (Equation (7)) was used to model the porosity curve, as shown in Figure 8c. The model predictions in all the sintering stages were satisfactorily accurate barring a small percentage of error. These model data will be employed in the next subsection dedicated to the finite element simulation of a 3D-printed cup shape.

4.6. Finite element simulation of the sintering shrinkage

The viscosity parameters and pore gas functions were imported in the finite element sintering model, whose local sintering behavior was represented by Equation (9). In addition, Figure 9a presents the four main production steps of the ceramic cup: i) shape conception, ii) shape slicing, iii) printing of the green shape using the robocasting method, and iv) sintering using the optimized cycle shown in Figure 6c. The resulting finite element sintering simulation is shown in Figure 9b and 9c. The porosity gradients were negligible, and the stress developed owing to gravity was concentrated at the intermediate height of the cup. The stress and

distortions of the shape were negligible in the current case because the specimen was relatively small (3 cm). However, this finite element tooling was highly appropriate for predicting the potential distortions of complex shapes with large dimensions and small wall thickness. This is particularly true for the liquid-phase sintering, where the distortion may be high [16]. The comparison of the simulated and experimental sintered dimensions is reported in figure 10. The dimensional simulation error is ~~mainly~~ below 6 % except for the dimension r_1 where the measurement is difficult.

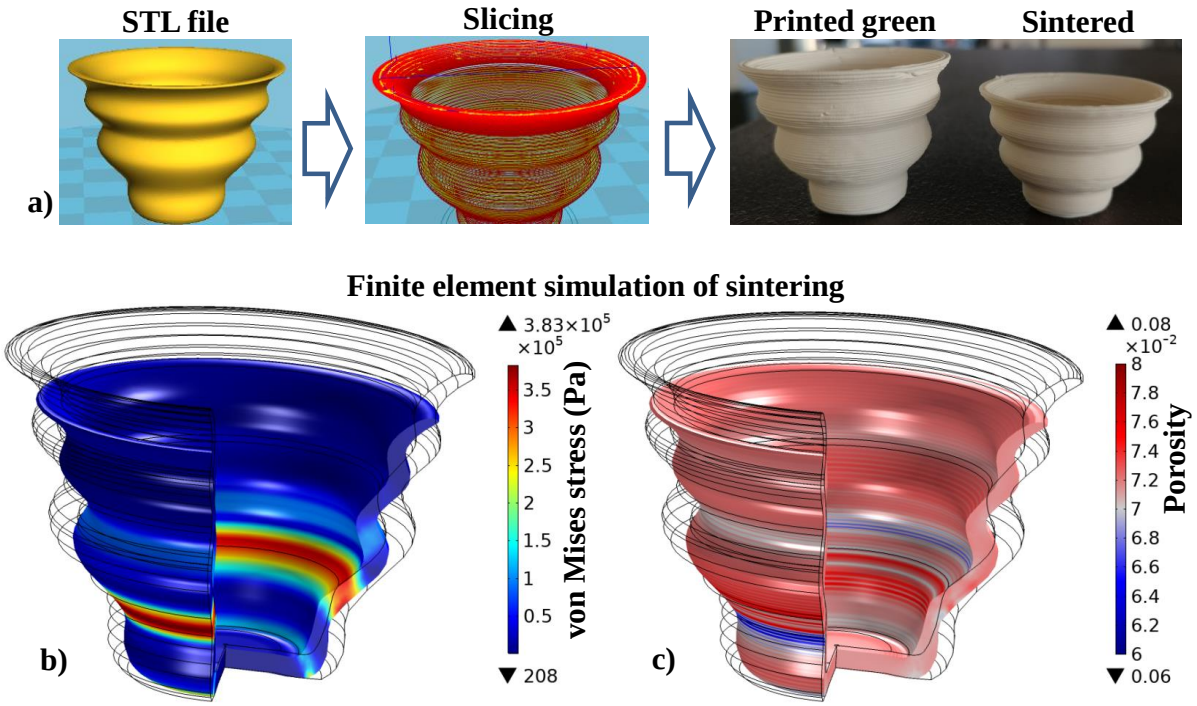

Figure 9 a) Robocasting of a ceramic 3D cup shape; b, c)sintering 2D axisymmetric finite element sintering simulation; the black lines correspond to the initial green geometry; (b) von Mises stress and (c) porosity.

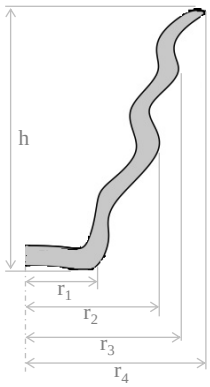

	EXP (mm)	SIM (mm)	Error (%)
h	28.24	27.59	2.30
r1	8.68	7.72	11.06
r2	16.16	15.35	5.01
r3	18.53	17.45	5.83
r4	20.82	20.34	2.31

Figure 10 Experimental vs simulated dimensions comparison.

5. Conclusion

In this study, the ceramic additive manufacturing of porcelain was investigated. The sintering stage of this production technology may suffer from distortions owing to gravity and the friction from the supports. Presently, additive manufacturing research is deeply oriented towards producing bioinspired shapes and highly complex light-weight structures that require a compromise between the shape–structure complexity and the sintering distortions. The simulation/identification methods developed in this study are useful tools for predicting the shape sensibility toward sintering distortions. This concept was illustrated in this work through the study of the porcelain material, which had an intrinsic high sensibility toward swelling in the final stage of sintering and exhibited pore growth generation and pore coalescence phenomena. The gas trapped in pores was the most probable factor responsible for the swelling phenomenon. Moreover, the dilatometric experimental data was used to optimize the sintering cycle, thus avoiding excessive swelling and pore growth phenomena. An analytical sintering modeling approach was employed to determine the viscosity and evolution of the trapped gas pressures at initial/intermediate and final stage sintering, respectively. Finally, the identified data from the analytical model were employed in the finite element analysis to predict the shrinkage and internal stress distribution in the cup shape. The dimensional error can be of 6 % but more accurate finite element simulation may be done by taking into account the anisotropy. The modeling method used in this study can be employed as a basis to predict the sintering behavior of 3D-printed complex shapes.

Acknowledgements

The help and support of Jérôme Lecourt and Christelle Bilot is gratefully acknowledged.

Data availability

The raw/processed data required to reproduce these findings cannot be shared at this time due to technical or time limitations.

Credit authorship contribution statement

Charles Manière: Conceptualization, Supervision, Modeling, Writing; **Christelle Harnois:** Conceptualization, Supervision, review & editing; **Sylvain Marinel:** Conceptualization, Supervision, review & editing.

References

[1] T. Chartier, A. Badev, Rapid Prototyping of Ceramics, in: Handb. Adv. Ceram., Elsevier, 2013: pp. 489–524. doi:10.1016/B978-0-12-385469-8.00028-9.

[2] J. Deckers, J. Vleugels, J.P. Kruth, Additive Manufacturing of Ceramics: A Review, J. Ceram. Sci. Technol. 5 (2014) 245–260. doi:10.4416/JCST2014-00032.

[3] Z. Chen, Z. Li, J. Li, C. Liu, C. Lao, Y. Fu, C. Liu, Y. Li, P. Wang, Y. He, 3D printing of ceramics: A review, J. Eur. Ceram. Soc. 39 (2019) 661–687. doi:10.1016/j.jeurceramsoc.2018.11.013.

[4] J.-C. Wang, H. Dommati, S.-J. Hsieh, Review of additive manufacturing methods for high-performance ceramic materials, Int. J. Adv. Manuf. Technol. 103 (2019) 2627–2647. doi:10.1007/s00170-019-03669-3.

[5] E. Peng, D. Zhang, J. Ding, Ceramic Robocasting: Recent Achievements, Potential, and Future Developments, Adv. Mater. 30 (2018) 1802404. doi:10.1002/adma.201802404.

[6] J.W. Halloran, Ceramic Stereolithography: Additive Manufacturing for Ceramics by Photopolymerization, Annu. Rev. Mater. Res. 46 (2016) 19–40. doi:10.1146/annurev-matsci-070115-031841.

[7] T. Chartier, V. Pateloup, C. Chaput, Manufacturing of ceramic parts by additive manufacturing technologies, Tech. l'ingénieur. N4807v1 (2018) 1–27. https://www.techniques-ingenieur.fr/base-documentaire/materiaux-th11/ceramiques-42578210/elaboration-de-pieces-ceramiques-par-fabrication-additive-n4807/.

[8] A. M'Barki, L. Bocquet, A. Stevenson, Linking Rheology and Printability for Dense and Strong Ceramics by Direct Ink Writing, Sci. Rep. 7 (2017) 6017. doi:10.1038/s41598-017-06115-0.

[9] E. Feilden, E.G.-T. Blanca, F. Giuliani, E. Saiz, L. Vandeperre, Robocasting of structural ceramic parts with hydrogel inks, J. Eur. Ceram. Soc. 36 (2016) 2525–2533. doi:10.1016/j.jeurceramsoc.2016.03.001.

[10] E. Peng, X. Wei, U. Garbe, D. Yu, B. Edouard, A. Liu, J. Ding, Robocasting of dense yttria-stabilized zirconia structures, J. Mater. Sci. 53 (2018) 247–273. doi:10.1007/s10853-017-1491-x.

[11] J. Jiang, X. Xu, J. Stringer, Support Structures for Additive Manufacturing: A Review, J. Manuf. Mater. Process. 2 (2018) 64. doi:10.3390/jmmp2040064.

[12] F. Bos, R. Wolfs, Z. Ahmed, T. Salet, Additive manufacturing of concrete in construction: potentials and challenges of 3D concrete printing, Virtual Phys. Prototyp. 11 (2016) 209–225. doi:10.1080/17452759.2016.1209867.

[13] M. Lasgorceix, E. Champion, T. Chartier, Shaping by microstereolithography and sintering of macro–micro-porous silicon substituted hydroxyapatite, J. Eur. Ceram. Soc. 36 (2016) 1091–1101. doi:10.1016/j.jeurceramsoc.2015.11.020.

[14] C. Manière, G. Kerbart, C. Harnois, S. Marinel, Modeling sintering anisotropy in ceramic stereolithography of silica, Acta Mater. 182 (2020) 163–171. doi:10.1016/j.actamat.2019.10.032.

[15] J.A. Alvarado-Contreras, E.A. Olevsky, R.M. German, Modeling of gravity-induced shape distortions during sintering of cylindrical specimens, Mech. Res. Commun. 50

(2013) 8–11. doi:10.1016/j.mechrescom.2013.02.007.
[16] J.A. Alvarado-Contreras, E.A. Olevsky, A.L. Maximenko, R.M. German, A continuum approach for modeling gravitational effects on grain settling and shape distortion during liquid phase sintering of tungsten heavy alloys, Acta Mater. 65 (2014) 176–184. doi:10.1016/j.actamat.2013.10.059.
[17] A.R. Khoei, Z. Molaeinia, S. Keshavarz, Modeling of hot isostatic pressing of metal powder with temperature–dependent cap plasticity model, Int. J. Mater. Form. 6 (2013) 363–376. doi:10.1007/s12289-012-1091-x.
[18] C. Manière, S. Chan, E.A. Olevsky, Microwave sintering of complex shapes: From multiphysics simulation to improvements of process scalability, J. Am. Ceram. Soc. 102 (2019) 611–620. doi:10.1111/jace.15892.
[19] C.-J. Bae, J.W. Halloran, Influence of Residual Monomer on Cracking in Ceramics Fabricated by Stereolithography, Int. J. Appl. Ceram. Technol. 8 (2011) 1289–1295. doi:10.1111/j.1744-7402.2010.02578.x.
[20] H. Li, L. Song, J. Sun, J. Ma, Z. Shen, Dental ceramic prostheses by stereolithography-based additive manufacturing: potentials and challenges, Adv. Appl. Ceram. 118 (2019) 30–36. doi:10.1080/17436753.2018.1447834.
[21] C. Manière, T. Zahrah, E.A. Olevsky, Fluid dynamics thermo-mechanical simulation of sintering: Uniformity of temperature and density distributions, Appl. Therm. Eng. 123 (2017) 603–613. doi:10.1016/j.applthermaleng.2017.05.116.
[22] E. Sánchez, J. García-Ten, V. Sanz, A. Moreno, Porcelain tile: Almost 30 years of steady scientific-technological evolution, Ceram. Int. 36 (2010) 831–845. doi:10.1016/j.ceramint.2009.11.016.
[23] R.L. Coble, Sintering Alumina: Effect of Atmospheres, J. Am. Ceram. Soc. 45 (1962) 123–127. doi:10.1111/j.1151-2916.1962.tb11099.x.
[24] M.N. Rahaman, Sintering of Ceramics, CRC Press, 2007.
[25] J. Martín-Márquez, J.M. Rincón, M. Romero, Effect of firing temperature on sintering of porcelain stoneware tiles, Ceram. Int. 34 (2008) 1867–1873. doi:10.1016/j.ceramint.2007.06.006.
[26] M. Biesuz, W.D. Abate, V.M. Sglavo, Porcelain stoneware consolidation by flash sintering, J. Am. Ceram. Soc. 101 (2018) 71–81. doi:10.1111/jace.15162.
[27] M.J. Orts, A. Escardino, J.L. Amorós, F. Negre, Microstructural changes during the firing of stoneware floor tiles, Appl. Clay Sci. 8 (1993) 193–205. doi:10.1016/0169-1317(93)90037-2.
[28] C.M. Riley, Relation of Chemical Properties to the Bloating of Clays, J. Am. Ceram. Soc. 34 (1951) 121–128. doi:10.1111/j.1151-2916.1951.tb11619.x.
[29] G. Petzow, M. Herrmann, Silicon Nitride Ceramics, in: High Perform. Non-Oxide Ceram. II, 2002: pp. 47–167. doi:10.1007/3-540-45623-6_2.
[30] C. Manière, E. Saccardo, G. Lee, J. McKittrick, A. Molinari, E.A. Olevsky, Swelling negation during sintering of sterling silver: An experimental and theoretical approach, Results Phys. 11 (2018) 79–84. doi:10.1016/j.rinp.2018.08.035.
[31] E.A. Olevsky, Theory of sintering: from discrete to continuum, Mater. Sci. Eng. R Reports. 23 (1998) 41–100. doi:10.1016/S0927-796X(98)00009-6.
[32] V.V. Skorohod, Rheological basis of the theory of sintering, Nauk. Dumka, Kiev. (1972).
[33] E.A. Olevsky, D. V. Dudina, Field-Assisted Sintering, Springer International Publishing, Cham, 2018. doi:10.1007/978-3-319-76032-2.
[34] W.M. Carty, U. Senapati, Porcelain Raw Materials, Processing, Phase Evolution, and Mechanical Behavior, J. Am. Ceram. Soc. 81 (1998) 3–20. doi:10.1111/j.1151-2916.1998.tb02290.x.
[35] M.S. Conconi, M. Morosi, J. Maggi, P.E. Zalba, F. Cravero, N.M. Rendtorff, Thermal behavior (TG-DTA-TMA), sintering and properties of a kaolinitic clay from Buenos Aires Province, Argentina, Cerâmica. 65 (2019) 227–235. doi:10.1590/0366-

69132019653742621.
[36] R.M. German, Sintering Theory and Practice, Wiley, Wiley, 1996. http://www.wiley.com/WileyCDA/WileyTitle/productCd-047105786X.html.
[37] E.A. Olevsky, C. Garcia-Cardona, W.L. Bradbury, C.D. Haines, D.G. Martin, D. Kapoor, Fundamental Aspects of Spark Plasma Sintering: II. Finite Element Analysis of Scalability, J. Am. Ceram. Soc. 95 (2012) 2414–2422. doi:10.1111/j.1551-2916.2012.05096.x.

Figure captions

Figure 1 Thermogravimetric (TG) and differential thermal analysis (DTA) curves of the powder under air atmosphere.

Figure 2 Constant heating rate sintering dilatometry curves of the printed specimens and in the insert the green fracture image showing not interlayer gaps.

Figure 3 Microstructure analysis of the dilatometry experiments.

Figure 4 EDS map of the porcelain specimen in the interlayer region.

Figure 5 EDS analysis of the different microstructures phases/regions.

Figure 6 Optimization sintering dilatometry tests with the corresponding microstructures (right) for 2 h holding; a) 2K/min, 1300 °C, b) 5 K/min, 1250°C, c) 1 k/min, 1200 °C.

Figure 7 Pore size histogram by pore surface frequency.

Figure 8 Sintering model parameters identification: a) viscosity parameters identification, b) pore gas pressure determination, and c) model verification.

Figure 9 a) Robocasting of a ceramic 3D cup shape; b, c)sintering 2D axisymmetric finite element sintering simulation; the black lines correspond to the initial green geometry; (b) von Mises stress and (c) porosity.

Figure 10 Experimental vs simulated dimensions comparison.